# In situ structures of RNA-dependent RNA polymerase inside bluetongue virus before and after uncoating

Yao He [a,b], Sakar Shivakotia,[b], Ke Ding [b], Yanxiang Cuia,[b], Polly Roy[c], and Z. Hong Zhou[a,b,1]

[a]Department of Microbiology, Immunology & Molecular Genetics, University of California, Los Angeles, CA 90095;

[b]California NanoSystems Institute, University of California, Los Angeles, CA 90095; and

[c]Department of Pathogen Molecular Biology, London School of Hygiene and Tropical Medicine, WC1E 7HT London, United Kingdom

[1]To whom correspondence may be addressed. Email: Hong.Zhou@UCLA.edu.

**Keywords:**

## ABSTRACT

Bluetongue virus (BTV), a major threat to livestock, is a multi-layered, nonturreted member of the Reoviridae, a family of segmented dsRNA viruses characterized by endogenous RNA transcription through an RNA-dependent RNA polymerase (RdRp). To date, the structure of BTV RdRp has been unknown, limiting our mechanistic understanding of BTV transcription and hindering rational drug de-sign effort targeting this essential enzyme. Here, we report the in situ structures of BTV RdRp VP1 in both the triple-layered virion and double-layered core, as determined by cryo-electron microscopy (cryoEM) and sub particle reconstruction. BTV RdRp has 2 unique motifs not found in other viral RdRps: a fingernail, attached to the conserved fingers subdomain, and a bundle of 3 helices: 1 from the palm subdomain and 2 from the N-terminal domain. BTV RdRp VP1 is anchored to the inner surface of the capsid shell via 5 asymmetrically arranged N termini of the inner capsid shell protein VP3A around the 5-fold axis. The structural changes of RdRp VP1 and associated capsid shell proteins between BTV virions and cores suggest that the detachment of the outer

capsid proteins VP2 and VP5 during viral entry induces both global movements of the inner capsid shell and local conformational changes of the N-terminal latch helix (residues 34 to 51) of 1 inner capsid shell protein VP3A, priming RdRp VP1 within the capsid for transcription. Understanding this mechanism in BTV also provides general insights into RdRp activation and regulation during viral entry of other multi-layered, non-turreted dsRNA viruses.

## Significance

Bluetongue virus (BTV) is a double-stranded RNA (dsRNA) virus that often causes significant economic damage to the livestock industry. The RNA-based genome transcription of BTV during infection depends on its RNA-dependent RNA polymerase (RdRp) inside the capsid. Here, we report a structure of BTV RdRp derived from cryo-electron microscopy (cryoEM) and reconstruction methods. The structure reveals how BTV RdRp interacts with associated genomic dsRNA and capsid proteins. Structural comparison between RdRp in the transcriptionally incompetent BTV virion and transcriptionally competent BTV cores provides insights into the highly regulated mechanism of mRNA transcription initiation. This structure of BTV RdRp and our mechanistic findings could now be exploited to design antivirals against the bluetongue disease in the livestock farming industry.

## Introduction

Bluetongue virus (BTV) is a member of the Orbivirus genus within the Reoviridae family, a large family of viruses that infect insects, plants, and animals, including humans (1). These nonenveloped viruses are characterized by a genome that comprises 9 to 12 segments of linear, double-stranded RNA (dsRNA) enclosed alongside multiple copies of an RNA-dependent RNA polymerase (RdRp) in an icosahedral capsid shell (2–4). They can be divided into 2 subfamilies, turreted (Spinareovirinae) and non-turreted (Sedoreovirinae), based on the presence or absence of turrets on their (inner) capsids.

As a nonturreted member of the family, BTV has 4 structural proteins organized into a triple-layered capsid: an outer layer composed of 60 triskelion-like VP2 trimers and 120 globular trimers of VP5 interdigitating one another, a middle layer of 260 VP7 trimers, and an inner layer formed by 60 dimers of the capsid shell protein VP3 (5–9).

Ten genomic dsRNA segments are compacted inside the capsid shell alongside enzymatic proteins, including putative helicase VP6 (10, 11), mRNA capping enzyme VP4 (12, 13), and RdRp VP1 (6, 14, 15). During cell entry, the VP2 protein binds receptors on the host cell surface and facilitates clathrin-mediated endocytosis of the BTV virion, while the VP5 protein penetrates the cell membrane and releases the double-layered particle, the core, into the host cytosol (8, 16). The BTV core remains intact in the cytosol with 10 genomic dsRNA segments encapsidated while avoiding the antiviral defense mechanisms of the host cell (14, 17). In the BTV core, the RdRp VP1 protein initiates endogenous transcription, using the negative strand of each genomic dsRNA segment as template, and then the newly synthesized positive-strand RNA transcripts are capped by capping enzyme VP4 and extruded into the host cytosol (14, 15, 18). These positive strands of RNA serve as mRNA for the translation of viral proteins within the cytoplasm. Subsequently, during virus assembly, the positive strands are packaged with newly synthesized capsid proteins to serve as the positive strand from which the complementary strand of the genomic dsRNA is replicated (19–21).

Icosahedral structures of the BTV virion and core have been determined to near-atomic resolution with X-ray crystallography and cryo-electron microscopy (cryoEM) (5, 8). However, what the structure of BTV RdRp VP1 is and how it interacts with the genome and other proteins are both unknown, significantly limiting our understanding of the RNA transcription mechanism inside BTV. The structures of RdRp and associated NTPase proteins have recently been determined by cryoEM for 2 turreted reoviruses: cytoplasmic polyhedrosis virus (CPV) (22, 23) and aquareovirus (ARV) (24, 25). However, as a nonturreted member of the Reoviridae, BTV does not contain an NTPase homolog, suggesting a different mechanism of virial transcription and assem-bly. The only known RdRp structure from a nonturreted member of the Reoviridae is that of rotavirus (26). Although its location inside the capsid shell has been studied by cryoEM (27–29), there is only limited understanding of how capsid proteins and RNA interact with RdRp to activate and regulate transcription in situ. In this study, we determined the in situ structures of BTV RdRp VP1 inside both the triple-layered BTV virion and the double-layered BTV core by cryoEM and subparticle re-construction methods. Our asymmetric reconstructions of the BTV vertex region reveal that RdRp VP1 is anchored to the inside surface of the inner capsid shell via 5 asymmetrically arranged N termini of the 5 VP3 molecules around it. The structural

changes of RdRp VP1 and its associated capsid pro-teins between the virions and the cores suggest that detachment of the outer proteins during viral entry induces both global movements of the capsid shell and local conformational changes of an interacting VP3, priming RdRp VP1 within the capsid for transcription. This mechanism provides general insights into RdRp activation and regulation during cell entry of multilayered, nonturreted reoviruses.

## Results

### Overall Structures

To obtain the in situ structure of BTV RdRp VP1, we recorded cryoEM images (SI Appendix, Fig. S1A) of purified intact BTV virions with a direct electron detector and carried out single-particle analysis for 3D reconstruction (SI Appendix, Fig. S2). Icosahedral reconstruction reveals a flower-shaped, 5-fold symmetric density under each 5-fold vertex of BTV virion (SI Appendix, Fig. S3 A and B), similar to those contributed by RdRp-containing transcriptional enzyme complexes in other members of the Reoviridae (25, 28). However, structural details of this RdRp density remained obscure due to symmetrization during icosahedral reconstruction, except for a few α-helices (SI Appen-dix, Fig. S3 A and B). To resolve the structure of RdRp VP1 and dsRNA genome around it, we boxed out each icosahedral vertex as a sub particle from particle images and carried out asymmetric sub particle reconstruction (SI Appendix, Fig. S2). Essentially, each sub particle's 5 possible symmetry-related orientations, predicted from the icosahedral symmetry, were classified to identify a single asymmetric orientation and then locally refined (30, 31). An asymmetric reconstruction (Fig. 1A) was obtained at an effective resolution of 3.7 Å by combining 244,063 vertex sub particles (SI Appendix, Fig. S1 C and D). Our asymmetric sub particle reconstruction of the vertex region reveals the organization of BTV RdRp VP1 and dsRNA densities around it (Fig. 1A and Movie S1). One RdRp VP1 alone is anchored to the inner capsid shell by N termini of the 5 VP3 molecules surrounding the icosahedral 5-fold axis (Fig. 1A). This organization differs from that of the turreted members of the Reoviridae, whose capsid-anchored transcriptional enzyme complex structures are heterodimers of an RdRp and an NTPase (22–25). Above these internal structures are 3 layers of capsid proteins, including the inner capsid shell formed by VP3 dimers, the middle layer of VP7 trimers, and the outermost layer containing the

receptor-binding protein VP2 and penetration protein VP5 (Fig. 1A and Movie S1). The structures of these capsid proteins resolved in our asymmetric reconstruction are similar to those previously resolved in icosahedral reconstructions (7, 8). Inside the capsid shell, the dsRNA genome exhibits as parallel fragments, which are tightly packed into several layers surrounding RdRp VP1 (Fig. 1A). Each dsRNA fragment is separated from its neighbors, in the same layer or in adjacent layers, by an average of ~27 Å (Fig. 1A). However, in general, the RNA densities are not well-resolved, especially the RNA fragments in front of RdRp VP1, as shown in Fig. 1B, indicating a mixture of different RNA conformations across different particles. One piece of RNA density, labeled as terminal RNA, binds at the upper region of RdRp VP1 (Fig. 1B).

**Atomic Model of RdRp VP1.**

Typical of a 3.7-Å-resolution cryoEM map, our subparticle asymmetric reconstruction resolves bulky amino acid side chains (Fig. 1 D and E), allowing us to build an atomic model of BTV RdRp VP1 (Fig. 2, SI Appendix, Fig. S1F, and Movie S2). Each RdRp VP1 consists of an N-terminal do-main (residues 1 to 387), a polymerase core domain (residues 388 to 935), and a C-terminal bracelet domain (residues 936 to 1302) (Fig. 2 A–D and SI Appendix, Fig. S4). Although this do-main organization is similar to that of the known RdRp structures of the Reoviridae (22, 24, 26, 32, 33), BTV RdRp VP1 contains a fingernail motif and a helix bundle motif, both of which have not been observed in any other viral RdRp structures (SI Appendix, Fig. S5). The polymerase core domain, sandwiched between the N-terminal domain and the C-terminal bracelet domains, consists of 3 subdomains, fingers, palm, and thumb, arranged in classical right-hand configuration (Fig. 2D). The catalytic site lies within a cavity in the center of RdRp VP1 and does not contain any visible RNA density (Fig. 2F), indicating that the polymerase remains quiescent in triple-layered BTV virion, as expected. Four channels connecting the catalytic cavity with the exterior are used for template entry (top), NTP entry (rear), transcript exit (bottom), and template exit (through the center of C-terminal bracelet domain in the front; Fig. 2 F and G). Notably, the C-terminal bracelet domain of RdRp VP1 in the quiescent BTV virion adopts an open conformation with the template exit channel wide open, a conformation similar to that of the bracelet domain in quiescent and primed ARV (24) and transcribing CPV (Fig. 2C), both turreted reoviruses.

The fingernail motif (residues 655 to 713) sits atop the fingers subdomain of BTV RdRp VP1 (Fig. 2D), representing an insertion into the characteristic β hairpin in the fingers subdomain (Fig. 2E and SI Appendix, Fig. S5) of other viral RdRp structures known to date. Flanking 1 side of the template entry channel, the fingernail motif possesses opposite electrical charge properties on its 2 sides (SI Appendix, Fig. S6). The positively charged side (SI Appendix, Fig. S6E) attaches to the edge of the N-terminal domain (SI Appendix, Fig. S6B) via strong electrostatic interactions, whereas the negatively charged side faces the dsRNA genome around RdRp VP1 (Fig. 2I and SI Appendix, Fig. S6D). On the other side of the template entry channel is a helix bundle motif consisting of 3 α-helices from the N-terminal domain (Nα2 and Nα3 in Fig. 2B) and the palm subdomain (Pα19 in Fig. 2D), a motif also absent in the known RdRp structures of other members of the Reoviridae (SI Appendix, Fig. S5).

Our in situ structure of the RdRp with bound RNA suggests a likely path of RNA during transcription. At the entrance to the template entry channel, the terminal RNA has a skinny end that binds residue H40 (SI Appendix, Fig. S7) of the helix bundle motif (Fig. 2G). This skinny end of the terminal RNA is likely the 5′ cap of the positive strand of a dsRNA genome segment. Such interaction between the 5′ cap and histidine residue is also observed in the structure of ARV RdRp in the primed state (24). In the initial step of transcription, the 5′ cap of the RNA positive strand may move further and interact with positively charged (region 1 in Fig. 2I) and aromatic (e.g., H183) residues in the cap-binding site (SI Appendix, Fig. S7), which is equivalent to the cap-binding sites observed in the RdRp structures of reovirus and rotavirus (22, 24, 26, 34). In such a scenario, the negative strand of the same terminal dsRNA could bind residue H48 on the other side (SI Appendix, Fig. S7) to facilitate splitting of the 2 RNA strands to initiate RNA transcription. Subsequently, the negative strand would slide through the template entry channel into the catalytic cavity to synthesize the nascent mRNA and exit through the template exit channel (Fig. 2 F and G). On the surface of RdRp VP1, a contiguous positively charged strip (region 2 to 3 in Fig. 2I), lined by negatively charged strips (regions 4 and 5 in Fig. 2I), forms a track to guide the movement of the RNA positive strand, leading to the reannealing of 2 RNA strands outside the template exit channel. This RNA pathway is similar to those visualized in the in situ structures of rotavirus RdRp during transcription (34, 35).

**Interactions between the N Termini of 5 VP3A Molecules and RdRp VP1.**

Our asymmetric subparticle reconstruction of the BTV vertex region resolves asymmetrically arranged N-terminal regions (residues are indicated in SI Appendix, Fig. S8) of the inner capsid protein VP3A (Fig. 3 and Movie S2), which, due to the imposition of symmetry, were invisible in both the icosahedral cryoEM reconstruction of the BTV virion (7, 8) and the X-ray crystal structure of the BTV core (5). The inner capsid of each BTV vertex consists of 5 VP3A-VP3B dimers (Fig. 3A). VP3A1–5 are arranged into a star-shaped structure, with their conserved apical domains forming the mRNA exit pore along the 5-fold axis, whereas VP3B1–5 are wedged between neighboring VP3As to complete the inner capsid shell (Fig. 3B). The newly resolved N-terminal fragment contains 1 α-helix connected to the rest of the VP3A model via a structurally variable loop (Fig. 3C). This variable loop allows the N-terminal segment of VP3A to adopt different conformations to reach and anchor RdRp VP1 under the inner capsid shell (Fig. 3 D–F).

Of the 5 N termini, that of VP3A1 (red) attaches to the outside surface of the N-terminal domain of RdRp VP1 (Fig. 3D), while the other 4 interact with the C-terminal bracelet domain (Fig. 3 E and F). The N-terminal β-strand of VP3A3 (yellow) augments 2 β-strands (Bβ1 and Bβ2 in SI Appendix, Fig. S4) of the C-terminal bracelet domain to form a 3-stranded antiparallel β-sheet (Fig. 3E), over which the N-terminal region of VP3A2 (orange) crosses to form another domain-swapped β-sheet (Fig. 3E). The negatively charged residues on the N-terminal loop of VP3A4 (green), including E19, D21, and D26, interact with the positively charged region (region 3 in Fig. 2I) close to the tem-plate exit channel of RdRp VP1 (Fig. 3F). The N-terminal helix of VP3A (blue) extends toward the 5-fold axis and inserts be-tween the inner capsid shell and Bα5 (SI Appendix, Fig. S4) of the C-terminal bracelet domain of RdRp VP1 to mediate their interactions (Fig. 3F). Notably, the contributing residues and helix length of the 5 N-terminal helices vary according to the relative position between VP3As and RdRp VP1 (SI Appendix, Fig. S8). The N-terminal helices of VP3A3 (yellow) and VP3A4 (green) are shorter than the others, and their connecting loops were invisible. These differences suggest that helices are partially unwound to generate longer loops to connect with RdRp VP1 (Fig. 3B). Similar to these observations in BTV, in situ cryoEM reconstructions of CPV and ARV also reveal that their transcriptional enzyme complexes (RdRp + NTPase) are anchored to the inner capsid shell by the N termini of capsid shell proteins (22, 24), indicating a conserved mechanism of RdRp-capsid

assembly among these viruses despite the existence of the NTPase in turreted reoviruses.

**Detachment of the External Proteins Triggers Conformational Change of RdRp VP1.**

Since RdRp VP1 in the BTV virion is incapable of mRNA transcription and becomes functional after the cell entry of the BTV core, we hypothesized that removal of the external proteins might trigger conformational change of RdRp VP1, thus priming it for the synthesis of mRNA. To test this hypothesis, we determined the in situ structure of RdRp VP1 inside the BTV core, obtained an asymmetrical subparticle reconstruction of the vertex region at 3.6 Å, and built atomic models of RdRp VP1 and associated N termini of VP3As (SI Appendix, Figs. S1, S9, and S10). Superposition of the vertex subparticle reconstructions of the virion and core shows that the inner capsid shell of the core expands through anisotropic movements (with respect to the center of the capsid) of all proteins (Fig. 4 A–C and Movie S3). The maximal movement (~6.5 Å) occurs at the apical domains of the VP3As surrounding the 5-fold axis, to which RdRp VP1s is anchored (Fig. 4C and SI Appendix, Fig. S11). Further comparison between the densities of RdRp VP1 in the virion and the core reveals that the C-terminal bracelet domain undergoes a conformational change, whereas the N-terminal domain and the polymerase core domain remain the same (Fig. 4 D and E). The most significant movement of the C-terminal bracelet domain involves the bracelet α helix Bα5, which shifts over 10 Å along the opposite direction of capsid movement (SI Appendix, Fig. S10).

Inserted between the inner capsid shell and the bracelet Bα5 (Fig. 3F), the N-terminal helix of VP3A5, which we termed the latch helix, mediates the outward movement of inner capsid shell and local conformational change of the C-terminal bracelet do-main during the priming process. Both the latch helix and the bracelet Bα5 are amphipathic helices, and their hydrophobic faces interact with each other, giving rise to a coiled coil structure (Fig. 4 G and L). In the virion, the hydrophilic face of the latch helix is attached to polar residues (e.g., R308 and S311) on the inner capsid shell (Fig. 4 G and H), stretching the C-terminal bracelet domain to adopt a tensed conformation (Fig. 4F). How-ever, during cell entry, detachment of outer capsid proteins in-duces the movement of the inner capsid shell and breaks the interaction between the latch helix and inner capsid protein VP3. Then, the latch helix and bracelet Bα5 move together (Fig. 4 J and K), changing the C-terminal bracelet domain to a relaxed con-formation

(Fig. 4I and Movie S3). The energy released in these processes might fuel the mechanical movement accompanying the initiation of mRNA transcription, and the increased volume inside the capsid would facilitate sliding of genomic dsRNA duplexes.

## Discussion

In this study, we have determined the structure of BTV RdRp by cryoEM and asymmetric, subparticle reconstruction. This structure and other known RdRp structures, including those in CPV (22, 23), MRV (32), ARV (24, 25), and rotavirus (26, 34, 35), share a similar 4-channeled architecture of RdRp with catalytic site buried in the cavity (SI Appendix, Fig. S5). However, BTV RdRp has 2 extra motifs, a fingernail and a helix bundle, that have not been observed in other RdRp structures. These 2 motifs are located near the template entry channel, making the channel deeper. The presence of the fingernail in BTV RdRp pushes the terminal RNA to approach the template entry channel in a slightly different orientation. The RdRp in turreted members of Reoviridae, including CPV, MRV, and ARV, contains 2 β hair-pins at the bottom part of the fingers subdomain (SI Appendix, Fig. S5). These β hairpins interact with an NTPase bound to the RdRp in the turreted viruses, but are missing in nonturreted viruses (e.g., BTV and rotavirus), which lack a bound NTPase, suggesting a correlation between the existence of β hairpins and the existence of a bound NTPase.

Viral transcription is highly regulated, as demonstrated bio-chemically and structurally in viruses in the family of Reoviridae (3, 36–40). In these viruses, mRNA transcription is activated by external actions, such as binding S-adenosyl-L-methionine in the single-layered CPV (3, 37, 38) and removing outer shell proteins in the multilayered reoviruses (36, 39, 40). However, how the removal of the outer capsid proteins triggers the initiation of transcription inside the capsid in multilayered reoviruses remains hitherto unknown. Although obvious differences exist in the buffer conditions of the current study and the native cytoplasmic environment encountered by transcriptionally active BTV during infection, our asymmetric reconstructions of the vertex regions of both triple-layered BTV virion and double-layered BTV core particles give us some indications of how the transcription signal is relayed from outside to inside.

Structural comparison between RdRp VP1 and associated inner capsid proteins in both BTV virion and BTV core particles suggests that the inner capsid shell protein

VP3A plays an important role in signal transduction. During viral entry, the removal of outer capsid proteins changes the curvature of the inner capsid shell, inducing an outward movement of inner capsid proteins VP3 around the 5-fold axis. This global movement breaks the interaction between the N-terminal helix of VP3A5 (the latch helix) and inner capsid shell, resulting in the local conformational change of the C-terminal bracelet domain of RdRp VP1. The energy released in these processes and volume enlargement inside the capsid might provide energy and space for the initiation of mRNA transcription. This signal-transduction mechanism from outside to inside might be shared by other members of multilayered reoviruses.

BTV infection of livestock can have significant economic and agricultural impacts on the farming industry (41, 42). Current countermeasures focus on developing life-attenuated live viruses as vaccines. As RdRp is an essential enzyme for viral replication, and transcription not shared by the host, it serves as a promising drug target. Indeed, the publication of X-ray structure of rotavirus RdRp has generated an impetus to structure-based drug design efforts in recent years (26, 43). The atomic structures of BTV RdRp presented here now open the door to design antivirals for therapeutic intervention against bluetongue virus infections.

## Materials and Methods

**Sample Preparation.** BSR cells were infected with BTV-1 at ~0.03 infectious units per cell and maintained at 35 °C for 2 more days postinfection. Infected cells were lysed in Tris buffer (100 mM Tris·HCl at pH 8.8, 50 mM NaCl, 10 mM EDTA) and 0.2% vol/vol Nonidet P-40 at 4 °C for 10 min. The lysate was centrifuged at 2,000g for 10 min to pellet nuclei. The supernatant was incubated at room temperature for 30 to 45 min after adding sodium deoxycholate to the final concentration of 0.1%. After the incubation, the supernatant was loaded onto a double cushion (4 mL 66% wt/wt su-crose and 10 mL 40% wt/vol sucrose in 20 mM Tris·HCl at pH 8.8, 0.2% vol/vol Nonidet P-40) and centrifuged at 100,000g for 1 h at 4 °C. Materials at the interface between the 2 sucrose cushions were collected, diluted 10-fold in 50 mM Tris·HCl buffer at pH 8.8 with 0.2% Nonidet P-40, and incubated in water bath at 35 °C for 45 min after adding N-lauroylsarcosine sodium salt to the final concentration of 0.1%. After the incubation, the material was subjected to centrifugation at 16,000g for 10 min at 10 °C to remove aggregates. Then the virion-containing supernatant was centrifuged at 80,000g for 1 h at 10 °C. The resulting pellet consisting of mostly of virions and some core particles was resuspended in 20 μL of 50 mM Tris·HCl at pH 8.8.

CryoEM Imaging and Data Processing. To prepare cryoEM grids, 2.5-μL aliquots of sample were applied to thin continuous carbon film on lacey grid, blotted with filter paper, and plunged into liquid ethane. The viruses were imaged with a Titan Krios 300 kV electron microscope equipped with a Gatan K2 Summit direct electron detector at a calibrated magnification of 36,764× (pixel size 0.68 Å). Dose-fractionated frames were 2× binned (pixel size, 1.36 Å) and aligned for beam-induced drift correction using UCSF MotionCorr2 (44). The defocus values of the micrographs were determined by CTFFIND4 (45) to be in the range of −1.1 μm and −3.7 μm.

The data processing workflow for the reconstruction of RdRp VP1 in BTV core particles is summarized in SI Appendix, Fig. S9. Briefly, the orientation and center parameters of each of the 27,951 high-quality BTV core particles were determined by RELION 2.1 (46) and used to guide the extraction of vertex subparticles with a published procedure (30, 31). After further re-finement, each vertex subparticle was expanded with C5 symmetry to get 5 related duplicates, and exhaustive 3D classification was conducted without



applying any symmetry. Five classes with clear secondary structure elements for RdRp VP1 were resolved. We selected vertex subparticles in 1 of the 5 asymmetric classes and removed duplications, resulting in 211,980 good vertex subparticles. Those subparticle images were subjected to another round of 3D classification to further improve the density of RdRp VP1. Fi-nally, 150,346 good vertex subparticles (44.8% of all vertex subparticles) were selected and used for local refinement in RELION. A 3.6-Å-resolution asymmetric cryoEM map of the vertex region of BTV core was obtained and selected as the final map for subsequent model building. The resolution of the cryoEM maps were estimated on the basis of the gold-standard FSC = 0.143 criterion (47). We followed the same icosahedral and subparticle reconstruction procedures to process the 2 datasets of BTV virion in-dependently (SI Appendix, Fig. S2). Selected good vertex subparticles from 2 datasets were combined together in the final step of local refinement. A total of 244,063 vertex subparticles were used to obtain asymmetric re-construction of the vertex region of BTV virion at an average resolution of 3.7 Å.

Please refer to SI Appendix for more detailed description of cryoEM im-aging and data processing.

Atomic Modeling, Model Refinement, and Graphics Visualization. The atomic models of BTV RdRp VP1 and the previously unmodeled N-terminal fragment of capsid shell protein VP3A1–5 were built de novo with Coot (48) and refined with PHENIX (49) by following the procedure detailed previously (50). Visualization of the atomic model, including figures and movies, are made by UCSF Chimera (51).

**ACKNOWLEDGMENTS.** We thank Cristina Celma and Xing Zhang for initial efforts in viral culturing and structural determination, respectively; and Titania Nguyen for editing the manuscript. This project is supported partly by grants from the NIH (AI094386 to Z.H.Z. and AI045000 to P.R.) and The Wellcome Trust (100218 to P.R.). We acknowledge the use of resources at the Electron Imaging Center for Nanomachines supported by University of California, Los Angeles, and grants from the NIH (1S10OD018111 and 1U24GM116792) and the National Science Foundation (DBI-1338135 and DMR-1548924).

**Author contributions:** Z.H.Z. designed research; Y.H., S.S., K.D., Y.C., and P.R. performed research; Y.H. and Z.H.Z. analyzed data; and Y.H. and Z.H.Z. wrote the paper.

The authors declare no conflict of interest.

This article is a PNAS Direct Submission. T.S.D. is a guest editor invited by the Editorial Board.



**Data deposition:** The cryoEM density maps have been deposited in the Electron Micros-copy Data Bank under accession codes EMD-20398 (RdRp VP1 in BTV virion) and EMD-20407 (RdRp VP1 in BTV core). The atomic coordinates have been deposited in the Protein Data Bank under accession codes 6PNS (RdRp VP1 in BTV virion) and 6PO2 (RdRp VP1 in BTV core).

## References

1. P. Roy, Orbiviruses. Fields Virology, D. M. Knipe, P. M. Howley, Eds. (Lippincott Williams & Wilkins, Philadelphia, 2013), vol. 1, pp. 1402–1423.

2. X. Zhang, L. Jin, Q. Fang, W. H. Hui, Z. H. Zhou, 3.3 A cryo-EM structure of a non-enveloped virus reveals a priming mechanism for cell entry. Cell 141, 472–482 (2010).

3. X. Yu, J. Jiang, J. Sun, Z. H. Zhou, A putative ATPase mediates RNA transcription and capping in a dsRNA virus. eLife 4, e07901 (2015).

4. A. J. Auguste et al., A newly isolated reovirus has the simplest genomic and structural organization of any reovirus. J. Virol. 89, 676–687 (2015).
5. J. M. Grimes et al., The atomic structure of the bluetongue virus core. Nature 395, 470–478 (1998).
6. E. L. Nason et al., Interactions between the inner and outer capsids of bluetongue virus. J. Virol. 78, 8059–8067 (2004).
7. X. Zhang et al., Bluetongue virus coat protein VP2 contains sialic acid-binding do-mains, and VP5 resembles enveloped virus fusion proteins. Proc. Natl. Acad. Sci. U.S.A. 107, 6292–6297 (2010).
8. X. Zhang et al., Atomic model of a nonenveloped virus reveals pH sensors for a co-ordinated process of cell entry. Nat. Struct. Mol. Biol. 23, 74–80 (2016).
9. P. Roy, Bluetongue virus structure and assembly. Curr. Opin. Virol. 24, 115–123 (2017). 10. N. Stäuber, J. Martinez-Costas, G. Sutton, K. Monastyrskaya, P. Roy, Bluetongue virus VP6 protein binds ATP and exhibits an RNA-dependent ATPase function and a heli-case activity that catalyze the unwinding of double-stranded RNA substrates. J. Virol.
71, 7220–7226 (1997).
11. E. Matsuo, K. Yamazaki, H. Tsuruta, P. Roy, Interaction between a unique minor protein and a major capsid protein of bluetongue virus controls virus infectivity. J. Virol. 92, e01784-17 (2018).
12. N. Ramadevi, N. J. Burroughs, P. P. C. Mertens, I. M. Jones, P. Roy, Capping and methylation of mRNA by purified recombinant VP4 protein of bluetongue virus. Proc. Natl. Acad. Sci. U.S.A. 95, 13537–13542 (1998).
13. G. Sutton, J. M. Grimes, D. I. Stuart, P. Roy, Bluetongue virus VP4 is an RNA-capping assembly line. Nat. Struct. Mol. Biol. 14, 449–451 (2007).
14. P. Gouet et al., The highly ordered double-stranded RNA genome of bluetongue virus revealed by crystallography. Cell 97, 481–490 (1999).
15. M. Boyce, J. Wehrfritz, R. Noad, P. Roy, Purified recombinant bluetongue virus VP1 exhibits RNA replicase activity. J. Virol. 78, 3994–4002 (2004).
16. M. Forzan, M. Marsh, P. Roy, Bluetongue virus entry into cells. J. Virol. 81, 4819–4827 (2007).
17. P. M. Barral et al., Functions of the cytoplasmic RNA sensors RIG-I and MDA-5: Key regulators of innate immunity. Pharmacol. Ther. 124, 219–234 (2009).
18. P. P. Mertens, J. Diprose, The bluetongue virus core: A nano-scale transcription ma-chine. Virus Res. 101, 29–43 (2004).

19. S. Lourenco, P. Roy, In vitro reconstitution of Bluetongue virus infectious cores. Proc. Natl. Acad. Sci. U.S.A. 108, 13746–13751 (2011).
20. P. Y. Sung, P. Roy, Sequential packaging of RNA genomic segments during the as-sembly of Bluetongue virus. Nucleic Acids Res. 42, 13824–13838 (2014).
21. T. Fajardo, Jr, P. Y. Sung, P. Roy, Disruption of specific RNA-RNA interactions in a double-stranded RNA virus inhibits genome packaging and virus infectivity. PLoS Pathog. 11, e1005321 (2015).
22. X. Zhang et al., In situ structures of the segmented genome and RNA polymerase complex inside a dsRNA virus. Nature 527, 531–534 (2015).
23. H. Liu, L. Cheng, Cryo-EM shows the polymerase structures and a nonspooled genome within a dsRNA virus. Science 349, 1347–1350 (2015).
24. K. Ding, L. Nguyen, Z. H. Zhou, In situ structures of the polymerase complex and RNA genome show how aquareovirus transcription machineries respond to uncoating. J. Virol. 92, e00774-18 (2018).
25. X. Wang et al., Structure of RNA polymerase complex and genome within a dsRNA virus provides insights into the mechanisms of transcription and assembly. Proc. Natl. Acad. Sci. U.S.A. 115, 7344–7349 (2018).
. X. Lu et al., Mechanism for coordinated RNA packaging and genome replication by rotavirus polymerase VP1. Structure 16, 1678–1688 (2008).
27. L. F. Estrozi, J. Navaza, Ab initio high-resolution single-particle 3D reconstructions: The symmetry adapted functions way. J. Struct. Biol. 172, 253–260 (2010).
28. L. F. Estrozi et al., Location of the dsRNA-dependent polymerase, VP1, in rotavirus particles. J. Mol. Biol. 425, 124–132 (2013).
29. J. P. Rickgauer, N. Grigorieff, W. Denk, Single-protein detection in crowded molecular environments in cryo-EM images. eLife 6, e25648 (2017).
30. S. L. Ilca et al., Localized reconstruction of subunits from electron cryomicroscopy images of macromolecular complexes. Nat. Commun. 6, 8843 (2015).
31. Y. T. Liu, J. Jih, X. Dai, G. Q. Bi, Z. H. Zhou, CryoEM structures of herpes simplex virus type 1 portal vertex and packaged genome. Nature 570, 257–261 (2019).
32. Y. Tao, D. L. Farsetta, M. L. Nibert, S. C. Harrison, RNA synthesis in a cage–Structural studies of reovirus polymerase lambda3. Cell 111, 733–745 (2002).
33. S. Venkataraman, B. V. L. S. Prasad, R. Selvarajan, RNA dependent RNA polymerases: Insights from structure, function and evolution. Viruses 10, E76 (2018).

34. K. Ding et al., In situ structures of rotavirus polymerase in action and mechanism of mRNA transcription and release. Nat. Commun. 10, 2216 (2019).
35. S. Jenni et al., In situ structure of rotavirus VP1 RNA-dependent RNA polymerase. J. Mol. Biol. 10.1016/j.jmb.2019.06.016 (2019).
36. A. J. Shatkin, J. D. Sipe, RNA polymerase activity in purified reoviruses. Proc. Natl. Acad. Sci. U.S.A. 61, 1462–1469 (1968).
37. Y. Furuichi "Methylation-coupled" transcription by virus-associated transcriptase of cytoplasmic polyhedrosis virus containing double-stranded RNA. Nucleic Acids Res. 1, 809–822 (1974).
38. Y. Furuichi, "Pretranscriptional capping" in the biosynthesis of cytoplasmic poly-hedrosis virus mRNA. Proc. Natl. Acad. Sci. U.S.A. 75, 1086–1090 (1978).
39. J. Borsa, M. D. Sargent, P. A. Lievaart, T. P. Copps, Reovirus: Evidence for a second step in the intracellular uncoating and transcriptase activation process. Virology 111, 191– 200 (1981).
40. D. L. Farsetta, K. Chandran, M. L. Nibert, Transcriptional activities of reovirus RNA polymerase in recoated cores. Initiation and elongation are regulated by separate mechanisms. J. Biol. Chem. 275, 39693–39701 (2000).
41. P. Roy, M. Boyce, R. Noad, Prospects for improved bluetongue vaccines. Nat. Rev. Microbiol. 7, 120–128 (2009).
42. N. J. Maclachlan, S. Zientara, W. C. Wilson, J. A. Richt, G. Savini, Bluetongue and epizootic hemorrhagic disease viruses: Recent developments with these globally re-emerging arboviral infections of ruminants. Curr. Opin. Virol. 34, 56–62 (2019).
43. M. Bassetto, J. Van Dycke, J. Neyts, A. Brancale, J. Rocha-Pereira, Targeting the viral polymerase of diarrhea-causing viruses as a strategy to develop a single broad-spectrum antiviral therapy. Viruses 11, E173 (2019).
44. S. Q. Zheng et al., MotionCor2: Anisotropic correction of beam-induced motion for improved cryo-electron microscopy. Nat. Methods 14, 331–332 (2017).
45. A. Rohou, N. Grigorieff, CTFFIND4: Fast and accurate defocus estimation from elec-tron micrographs. J. Struct. Biol. 192, 216–221 (2015).
46. S. H. Scheres, RELION: Implementation of a bayesian approach to cryo-EM structure determination. J. Struct. Biol. 180, 519–530 (2012).
47. P. B. Rosenthal, R. Henderson, Optimal determination of particle orientation, abso-lute hand, and contrast loss in single-particle electron cryomicroscopy. J. Mol. Biol. 333, 721–745 (2003).

48. P. Emsley, B. Lohkamp, W. G. Scott, K. Cowtan, Features and development of Coot. Acta Crystallogr. D. Biol. Crystallogr. 66, 486–501 (2010).
49. P. D. Adams et al., PHENIX: A comprehensive python-based system for macromolec-ular structure solution. Acta Crystallogr. D. Biol. Crystallogr. 66, 213–221 (2010).
50. I. Yu et al., Building atomic models based on near atomic resolution cryoEM maps with existing tools. J. Struct. Biol. 204, 313–318 (2018).
51. E. F. Pettersen et al., UCSF Chimera–A visualization system for exploratory research and analysis. J. Comput. Chem. 25, 1605–1612 (2004).

## Conflict of interest

The authors declare no conflict of interest with the contents of this article.

## Author Contributions

SKR, PR designed the experiments; SKR, AK, BPM and YH performed the experiments; SKR, PR and ZHZ analysed data. SKR, PR and ZHZ wrote the manuscript.

## Figure legends

**Figure 1.** CryoEM reconstruction of the vertex region of BTV virion. (A) Su-perposition of the subparticle reconstruction of BTV vertex (colored) and the icosahedral reconstruction of BTV virion (gray), showing the relative loca-tions of the genomic RNA and individual proteins. The RNA densities are lowpass-filtered and radially colored. See also Movie S1. (B and C) CryoEM density map of RdRp VP1 and associated RNA shown in 2 orthogonal views. Nonassociated RNA densities are removed for clarity. (D and E) Close-up views of an α helix (D) and a loop (E) of RdRp VP1. Atomic models are shown as ribbons or sticks and cryoEM density as meshes.

**Figure 2.** In situ structure of RdRp VP1. (A–D) Ribbon representation of the atomic model of BTV RdRp VP1 showing in full (A) and as separate domains: N-terminal domain (B) C-terminal bracelet domain (C) and polymerase core domain (D). See also Movie S2. (C, Right) Ribbon models of the CPV bracelet domain in both quiescent and transcribing states (22) are shown, with corresponding modules highlighted for comparison. (E) Ribbon model of CPV polymerase domain (22). Comparison between BTV (D) and CPV (E) polymerase domains shows the fingernail motif (cyan) atop the BTV fingers subdomain (blue). (F–G) CryoEM density maps of RdRp VP1 alone (F)

and with terminal RNA binding (G) showing the 4 channels: template entry, template exit, NTP entry, and tran-script exit. Densities in G are lowpass-filtered to better show the RNA density. (H–I) Coulomb poten-tial surfaces of RdRp VP1 in 2 different views. De-pictions of BTV RdRp VP1 in A, D, F, and H are all in the same orientation..

**Figure 3.** Interactions between BTV RdRp VP1 and the N termini of 5 VP3A molecules, VP3A1–5. (A) CryoEM density map of 5 copies of VP3 dimers (VP3A+VP3B) and RdRp VP1, viewed from the inside of the inner capsid. (B) Ribbon diagrams of VP3A, VP3B, and RdRp VP1 in the same orientation as in A. VP3A1–5 con-formers are shown in light gray, with their N termini colored as in A. (C) Superposition of 5 VP3 dimers showing different conformations of VP3A N-terminal fragments. (D–F) Zoom-in views of interactions be-tween individual N termini of 5 VP3A and RdRp VP1 from 3 directions as indicated by the eye symbols in B. See also Movie S2.

**Figure 4**. Structural comparison of the vertex regions in BTV virion and BTV core showing global protein movements and local conformational changes. (A) CryoEM density of RdRp VP1 and inner capsid shell of BTV virion. (B) Superposition of RdRp VP1 and inner capsid shell between BTV core (gray) and BTV virion (colored by protein as in Fig. 1B). Both maps are lowpass-filtered to 6 Å and aligned to their corre-sponding icosahedral reconstructions as reference, before superposition. See also Movie S3. (C) Schematic illustration of B with the proteins in BTV core shown as gray outline. (D–E) Comparison of RdRp VP1 densities in BTV virion (D) and BTV core (E). Densities of the C-terminal bracelet domain in 2 maps are marked with red boxes. (F–K) Ribbon diagram of RdRp VP1 (purple) and the inner capsid protein VP3 (cyan) in BTV virion (F–H) and BTV core (I–K). Bα5 (purple) in the C-terminal bracelet domain of RdRp VP1 and the N-terminal helix of VP3A5 (blue, latch helix) are highlighted in G, H, J, and K. (L) Helical wheel representation of bracelet Bα5 and the latch helix of VP3A5 at a view similar to that of (H). Hydrophobic and polar residues are colored in gray and orange, respectively.

**Figure 1**

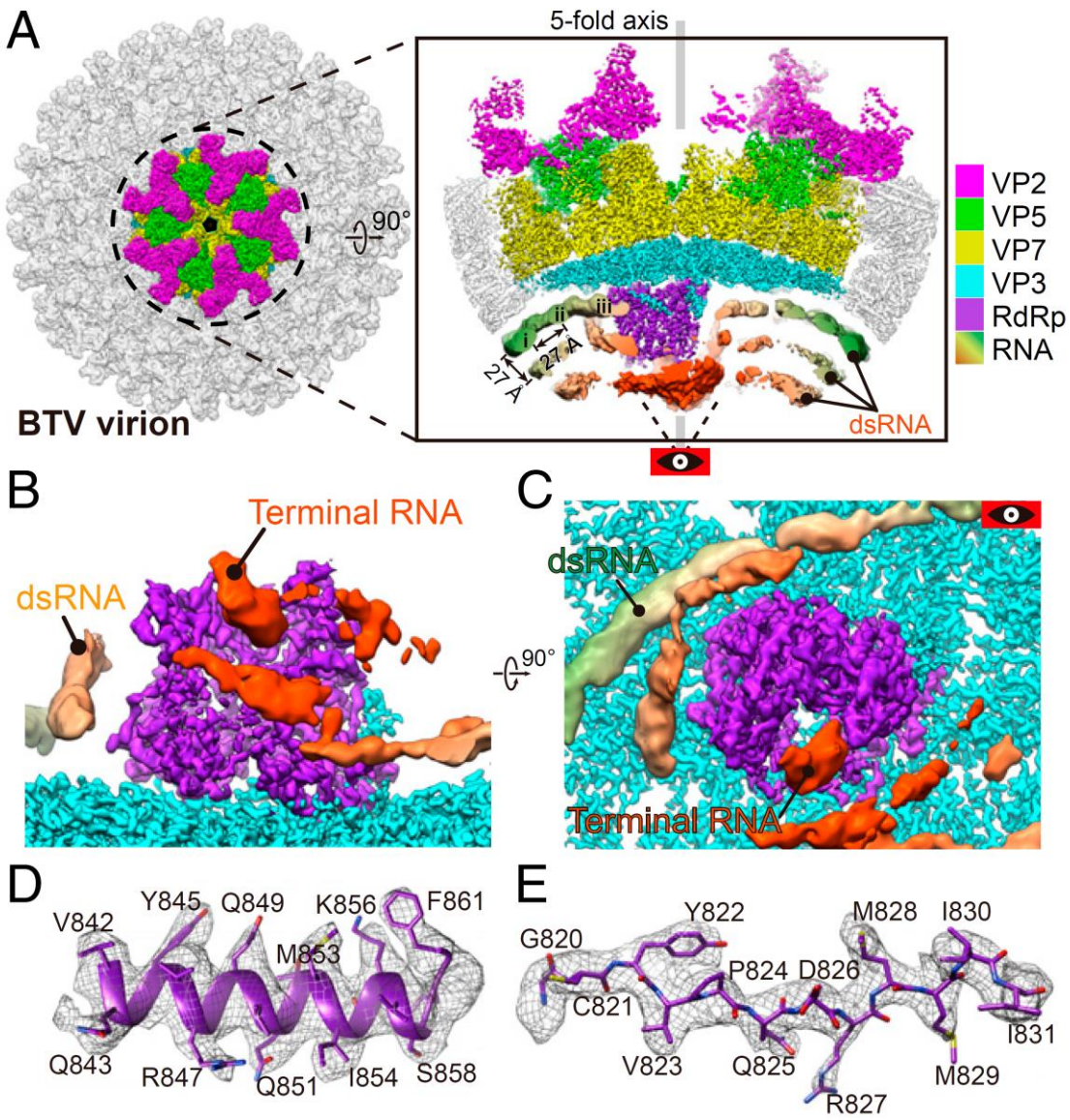
A
5-fold axis
90°
BTV virion
i
ii
iii
27 Å
27 Å
dsRNA
VP2
VP5
VP7
VP3
RdRp
RNA
B
Terminal RNA
dsRNA
C
dsRNA
90°
Terminal RNA
D
V842
Y845
Q849
K856
F861
M853
Q843
R847
Q851
I854
S858
E
G820
Y822
M828
I830
P824
D826
C821
I831
V823
Q825
M829
R827

**Figure 2**

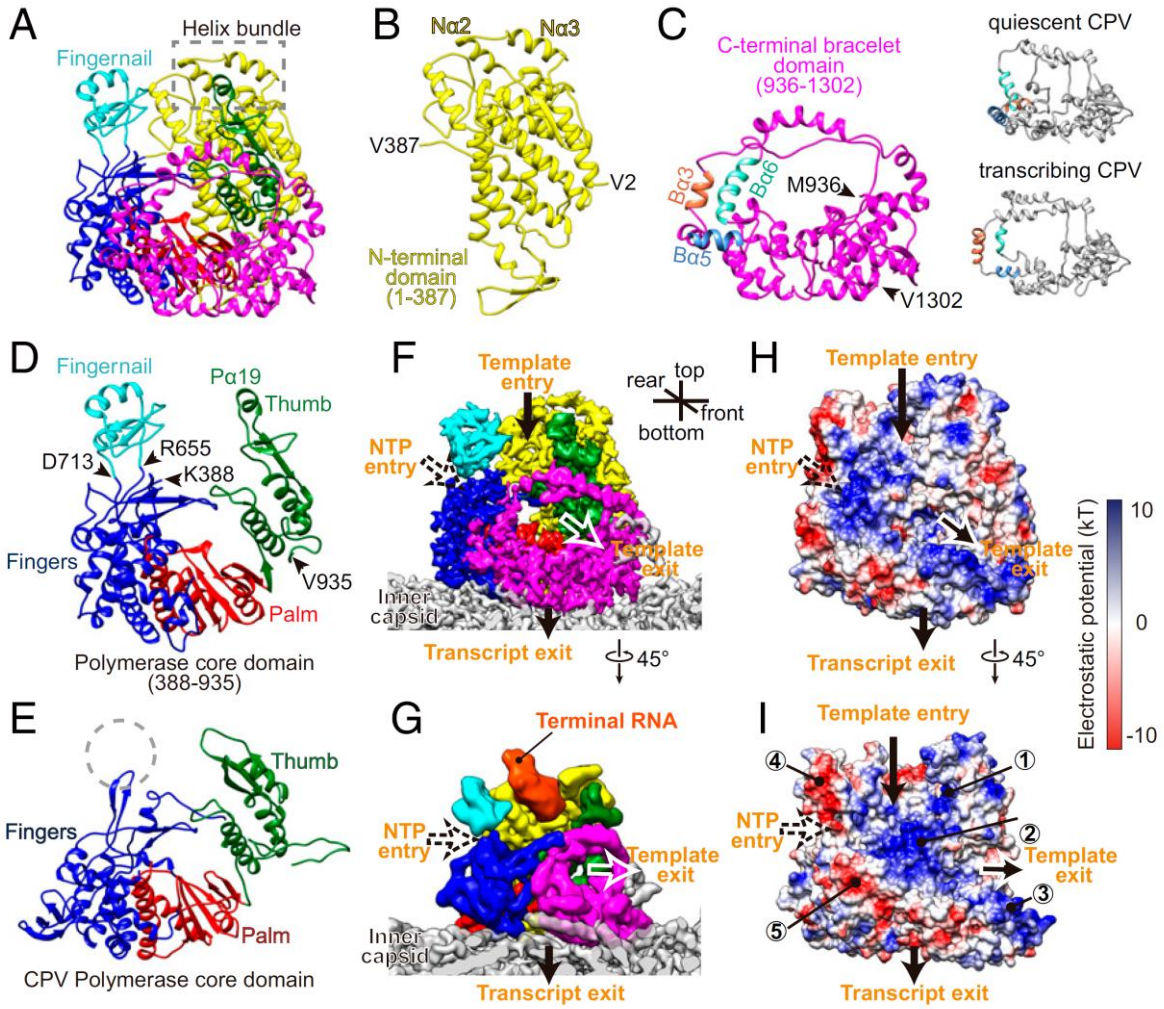
A
Helix bundle
Fingernail
B
Nα2
Nα3
V387
V2
N-terminal domain (1-387)
C
C-terminal bracelet domain (936-1302)
Bα3
Bα6
Bα5
M936
V1302
quiescent CPV
transcribing CPV
D
Fingernail
Pα19
Thumb
D713
R655
K388
Fingers
V935
Palm
Polymerase core domain (388-935)
E
Thumb
Fingers
Palm
CPV Polymerase core domain
F
Template entry
rear
top
front
bottom
NTP entry
Template exit
Inner capsid
Transcript exit
45°
G
Terminal RNA
NTP entry
Template exit
Inner capsid
Transcript exit
H
Template entry
NTP entry
Template exit
Transcript exit
45°
Electrostatic potential (kT)
10
0
-10
I
Template entry
NTP entry
Template exit
Transcript exit
①
②
③
④
⑤

**Figure 3**

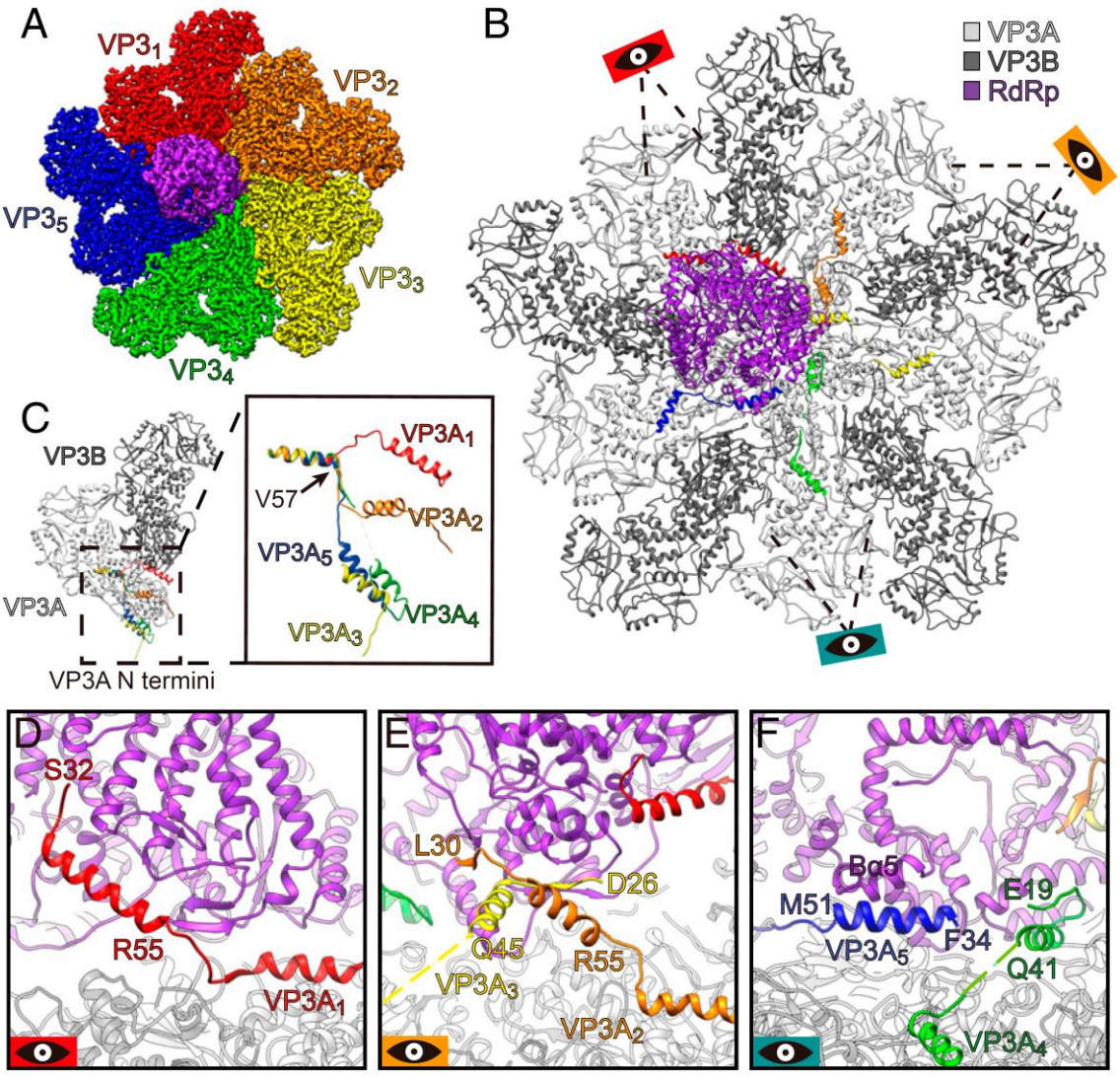
A
VP3$_1$
VP3$_2$
VP3$_5$
VP3$_3$
VP3$_4$
B
VP3A
VP3B
RdRp
C
VP3B
VP3A
VP3A N termini
V57
VP3A$_1$
VP3A$_2$
VP3A$_5$
VP3A$_4$
VP3A$_3$
D
S32
R55
VP3A$_1$
E
L30
D26
Q45
R55
VP3A$_3$
VP3A$_2$
F
Bα5
M51
E19
VP3A$_5$
F34
Q41
VP3A$_4$

**Figure 4**

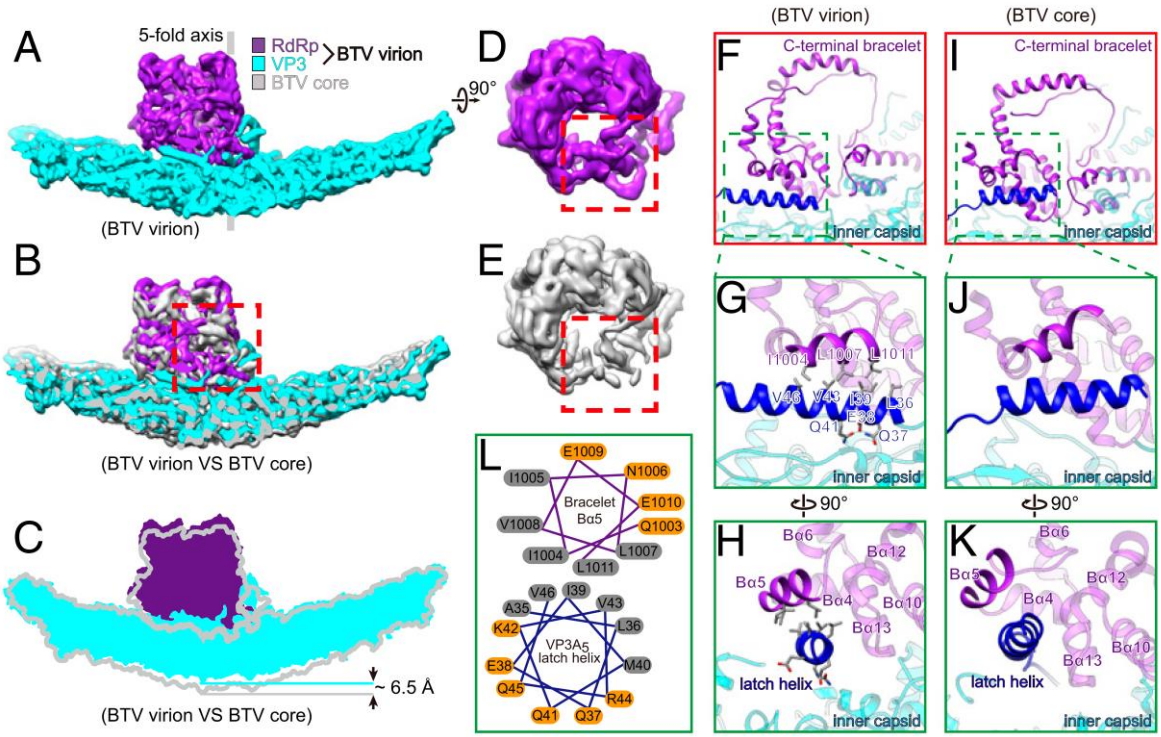
A
5-fold axis
RdRp
VP3
BTV core
BTV virion
(BTV virion)
B
(BTV virion VS BTV core)
C
~ 6.5 Å
(BTV virion VS BTV core)
D
90°
E
L
E1009
N1006
I1005
Bracelet
Bα5
E1010
V1008
Q1003
I1004
L1007
L1011
V46
I39
V43
A35
K42
L36
VP3A5
latch helix
E38
M40
Q45
R44
Q41
Q37
(BTV virion)
(BTV core)
F
C-terminal bracelet
inner capsid
I
C-terminal bracelet
inner capsid
G
I1004
L1007
L1011
V46
V43
I39
L36
E38
Q41
Q37
inner capsid
J
inner capsid
90°
90°
H
Bα6
Bα12
Bα5
Bα4
Bα10
Bα13
latch helix
inner capsid
K
Bα6
Bα5
Bα12
Bα4
Bα10
Bα13
latch helix
inner capsid